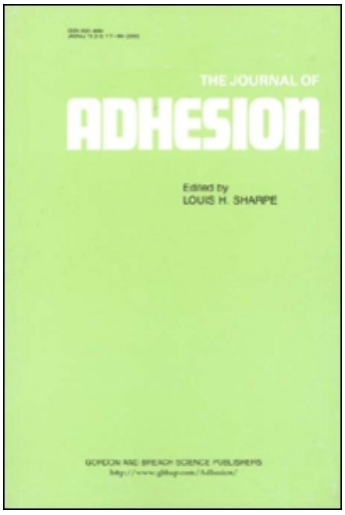

The Journal of Adhesion
Publication details, including instructions for authors and subscription information:
http://www.informaworld.com/smpp/title~content=t713453635

Critical Tractions for Initiating Adhesion Failure at Interfaces in Encapsulated Components

Douglas B. Adolf[a]; Robert S. Chambers[b]; Mark E. Stavig[a]; Stacie T. Kawaguchi[a]
[a] Materials and Process Sciences Center, Sandia National Laboratories, Albuquerque, New Mexico, USA [b] Engineering Sciences Center, Sandia National Laboratories, Albuquerque, New Mexico, USA

To cite this Article Adolf, Douglas B. , Chambers, Robert S. , Stavig, Mark E. and Kawaguchi, Stacie T.(2006) 'Critical Tractions for Initiating Adhesion Failure at Interfaces in Encapsulated Components', The Journal of Adhesion, 82: 1, 63 — 92
To link to this Article: DOI: 10.1080/00218460500418607
URL: http://dx.doi.org/10.1080/00218460500418607

The Journal of Adhesion, 82:63–92, 2006

ISSN: 0021-8464 print/1545-5823 online
DOI: 10.1080/00218460500418607

Taylor & Francis
Taylor & Francis Group

Critical Tractions for Initiating Adhesion Failure at Interfaces in Encapsulated Components

Douglas B. Adolf
Materials and Process Sciences Center, Sandia National Laboratories, Albuquerque, New Mexico, USA

Robert S. Chambers
Engineering Sciences Center, Sandia National Laboratories, Albuquerque, New Mexico, USA

Mark E. Stavig
Stacie T. Kawaguchi
Materials and Process Sciences Center, Sandia National Laboratories, Albuquerque, New Mexico, USA

Determining the initiation of adhesive failure at a surface buried deep within the bulk of an epoxy is qualitatively different from measuring the propagation of an existing surface crack. Most current tests are shown to be unsuitable for assessing the critical traction at initiation. A new test geometry is presented that initiates failure away from an air interface, produces a slowly varying stress distribution near the initiation site and minimal contributions from thermal residual stresses, and enables tests with mixed modes of loading. This new geometry is used to examine temperature-dependent adhesive failure in tensile, shear, and mixed modes of loading for both smooth and rough surfaces. Some of the experimental results are unexpected. As examples, the critical traction at initiation of adhesive failure is apparently insensitive to surface roughness, and the critical normal traction is independent of temperature while the critical tangential traction tracks the shear yield stress.

Keywords: Adhesion; Epoxy; Failure; Initiation; Test

Received 17 April 2005; in final form 1 September 2005.

Sandia is a multiprogram laboratory operated by Sandia Corporation, a Lockheed Martin Company, for the U.S. Department of Energy's National Nuclear Security Administration under Contract DE-AC04-94AL85000.

Address correspondence to Douglas B. Adolf, Materials and Process Sciences Center, Sandia National Laboratories, Albuquerque, NM 87185-0888. E-mail: dbadolf@sandia.gov

1. INTRODUCTION

Envision an electrical component that is encapsulated in an epoxy (Figure 1) to provide electrical and mechanical protection. Given an accurate polymer constitutive equation [1, 2], the stresses and strains in this component can be calculated, and design variations can be compared simply by examining the stress magnitudes (lower stresses imply a more robust design). However, design margins cannot be estimated because stress calculations by themselves do not predict failure. Ideally, adhesive and cohesive metrics of failure would be extracted from the predicted stresses and strains to determine when the loading level becomes critical. Because failure may initiate anywhere in a component, these failure metrics must be applicable for all temperatures, rates, geometries, and substrates encountered. This ambitious goal has yet to be realized. In the following article, we focus on paths toward consistent prediction of the initiation of adhesive failure at interfaces buried within an epoxy.

The profound difference between modeling the *initiation* of adhesive failure and modeling the *propagation* or stability of an existing interfacial crack may not be sufficiently appreciated. Examine the enlargement of the corner interface in the encapsulated component of Figure 1. With an appropriate radius of curvature and surface finish,

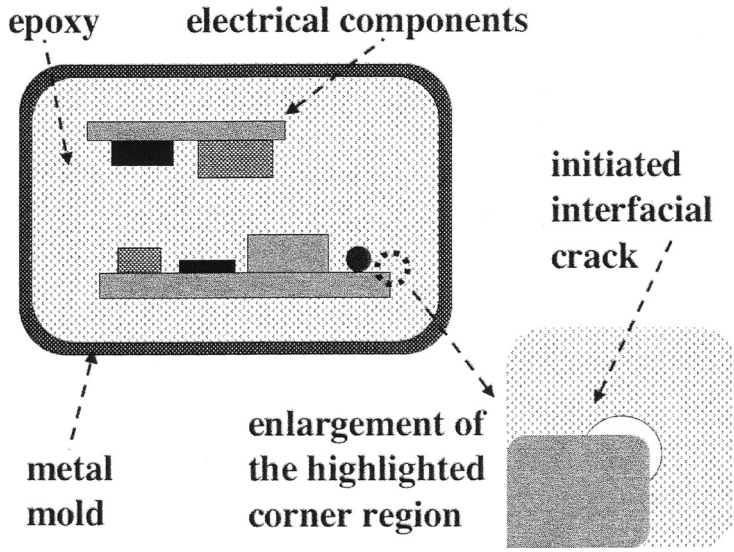

FIGURE 1 An idealized electrical component encapsulated in an epoxy.

the epoxy will adhere to this particular corner during cure. However, tensile stresses may develop during cool-down from the epoxy-cure temperature as the high coefficient of thermal expansion of the epoxy relative to the metal mold causes the epoxy to shrink. Notice that no interfacial cracks are seen initially. Because both the geometry of the component and the constitutive response of the materials are known, the stresses can be calculated fairly accurately subject to the assumptions of smooth interfaces and a continuum view of the epoxy. At some point, these stresses produce a traction on the curved surface that will cause debonding.

At this stage, the fidelity of the computational simulation is severely degraded. Although the mesh resolution might have been fine enough to capture the continuum epoxy stresses fairly accurately along the bonded corner, the crack now poses a much more severe geometrical problem. Typical finite-element simulations would model this propagating crack with an infinitely sharp tip. Yet, the realistic interfacial crack shape is much more complex and would require an inordinately fine mesh to resolve the actual physical features (*e.g.*, crack-tip blunting). Because no such mesh refinement is practical, the stresses at the crack tip cannot be computed accurately; in fact, the calculated stresses near the tip will be quite wrong using the original uncracked mesh. Therefore, techniques have been developed that do not require exact calculation of these tip stresses (*e.g.*, the J-integral approach [3]), allowing quasi-static extension of the sharp crack to determine if a debonding area of some size is stable [4–7]. Less commonly, transient dynamic analyses are used to model the actual propagation of a sharp crack [8]. Unfortunately, the price paid for such simplification of the physics typically shows up as more complicated functional forms of the phenomenological relationships required to match all experimental data. Specifically, failure metrics (*e.g.*, K_{IC} or J_{IC}) derived from such simplified models might depend on temperature, rate, and loading mode. By incorporating higher fidelity models and more physically based metrics of failure, one might be able to predict these dependencies naturally.

Our investigations focus only on quantifying the initiation of adhesive failure at interfaces surrounded by polymer. Nevertheless, in many applications, prediction of the initiation event in such components is itself sufficient for assessing design margins. For example, epoxy encapsulants are often used to provide protection from dielectric breakdown, and the presence of any surface crack is, at the very least, undesirable. Knowledge of the critical adhesive traction would highlight marginal designs and allow optimization of a component design that is far from any debonding event. Yet, as described in the previous

discussions, no crack exists prior to initiation, and debonding may occur at any surface with arbitrary geometry, even on a relatively flat surface where no appreciable stress risers are present and fracture mechanics–based approaches would be inapplicable. Therefore, a new approach is necessary that can be embedded within a computational simulation and would be applicable for all geometries. Ideally, component geometries would be meshed as accurately as possible, stresses would be calculated with high-fidelity constitutive equations, and metrics of debonding would determine when adhesive failure initiates. In this article, we (1) describe the connection between this type of approach and current traction–separation laws, (2) reference a new constitutive equation capable of predicting nonlinear glassy polymer response under all loading conditions and temperatures, (3) demonstrate a need for new tests from which metrics of debonding can be cleanly extracted, and (4) describe a new test geometry and show results using it.

Just as "initiation" needed clarification, so does the phrase "adhesive failure." Interfaces are obviously not mathematical planes cleanly dividing a substrate from the polymer. A complex "interphase" regime exists where the polymer density varies. In addition, the substrate is rarely molecularly smooth but, instead, can be quite rough. By adopting an engineering approach, adhesive failure could be taken to mean any failure near a smooth surface that produces a distinctively clean failure surface upon examination after testing. It would be irrelevant at this level to distinguish between failures that occurred exactly at the substrate or in the "interphase." Yet even this crude definition is limited. For example, a roughened surface tested in shear could actually initiate failure at the surface, but the ensuing propagating crack undoubtedly would not cleanly follow the substrate. Rather, it would "skim" across the peak features in a more cohesive fashion. In this case, the initiation event was assumed to be adhesive, yet the failure surfaces bear resemblance to cohesive fracture. One might suggest that adhesive failure be defined as any failure "near" the surface. Rather than quibble over definitions, perhaps it is better to focus on the ability to predict failure consistently that occurs between dissimilar materials.

2. COMPUTATIONAL MODELS FOR PREDICTING ADHESIVE FAILURE

Recent approaches that focus on predicting adhesive failure typically employ traction–separation laws [4–8]. Traction–separation laws are relationships attributed to interfacial rupture surfaces that enable

both initiation and propagation of cracks within a finite-element analysis. The traction, t, with units of stress, is a function of the displacement difference, δ, for two initially coincident points on the interface that separate during failure. Both of these vectors have components normal and tangential to the interface. Although quite complicated laws have been postulated, the simplest law is given by

$$t = \mathrm{f}\left(\frac{|\delta|}{\delta_\mathrm{C}}\right)\frac{\delta}{|\delta|}$$

where

$$\begin{aligned}\mathrm{f}\left(\frac{|\delta|}{\delta_\mathrm{C}}\right) &= 2\,t_{\max}\frac{|\delta|}{\delta_\mathrm{C}} \quad \text{for} \quad 0 \le |\delta| \le \frac{\delta_\mathrm{C}}{2} \\ &= 2\,t_{\max}\left(1 - \frac{|\delta|}{\delta_\mathrm{C}}\right) \quad \text{for} \quad \frac{\delta_\mathrm{C}}{2} \le |\delta| \le \delta_\mathrm{C}\end{aligned} \tag{1}$$

where the traction vanishes at a critical magnitude of the displacement vector, δ_C.

Examine Equation (1) for an intact interface in a ramped tensile test. The sample would irreversibly separate in this test when the magnitude of the normal traction reached a value of $t_{\max}$. This value of $t_{\max}$, then, is the model parameter characterizing the initiation of adhesive failure in this type of test. However, Equation (1) contains an additional parameter, δ_C. The work associated with pulling the two surfaces completely apart would be

$$W_\mathrm{s} = \frac{1}{2}t_{\max}\delta_\mathrm{C} \tag{2}$$

so the value of the critical displacement magnitude can be determined by measuring the work of separation. Therefore, even the simplest traction–separation law of Equation (1) has two independent parameters that could be chosen to predict both initiation ($t_{\max}$) and propagation (W_s). From the discussions in the Introduction, one might believe that the parameter associated with initiation, $t_{\max}$, is somewhat more "fundamental" than the propagation parameter, W_s, which must be quite phenomenological because stresses are not calculated accurately after initiation.

If one is interested solely in predicting the initiation of adhesive failure in monotonically ramped tests and not carrying the calculations further to predict propagation of the interfacial crack, use of the traction–separation law in Equation (1) is practically indistinguishable from initiating failure at a critical surface traction magnitude, $t_{\max}$, computed directly from the finite-element stress

analysis. That is, the traction at a surface can be calculated directly from the element stresses, $\underline{\sigma}$ as

$$t = \sigma \cdot n \tag{3}$$

where n is the unit vector normal to the surface. Assigning the initiation of adhesive failure to a critical value of this traction, $t_{\max}$, is then perhaps not mathematically equivalent but practically identical to predicting initiation with Equation (1) in these tests.

A slightly more complicated but more realistic model for initiation of adhesive failure would allow independent values of the critical traction normal and tangential to the surface. The traction would still be computed as in Equation (3), but debonding would initiate in shear at a value of $t_{\max}^{\text{tang}}$ and in tension at a tensile value of $t_{\max}^{\text{norm}}$. More generally, a critical traction-failure envelope would be defined using at least these two values. It is possible that the critical values could depend upon temperature and rate of deformation.

The proposed approach of predicting the initiation of adhesive failure by using finite-element analyses to predict accurately the stresses that, in turn, define failure metrics for debonding is compatible with current traction–separation laws. The metrics of debonding, in this case, would simply be defined by the critical traction envelope. Still required are tests from which these metrics can be extracted cleanly, and defining these tests is the main purpose of this article.

3. TESTS FOR EXTRACTING THE CRITICAL MODEL PARAMETERS

3.1. Historical Tests

Tests are required to extract at least two parameters, the values of the traction at failure under pure shear and under pure tension. Numerous adhesive tests have been proposed, but most are fundamentally flawed for assessing the required metrics for initiation at embedded interfaces. Perhaps the most common and easily discussed tests of this class are butt tensile and lap shear. The stresses in both of these samples are often assumed to be homogeneous; for example, the applied load at failure per sample area in butt tensile is equated to the critical normal traction. The stresses, of course, are nowhere near homogeneous in these samples. Rather, initiation always occurs at the corners where the stress is greatly intensified. In fact, the high stress at these corners can be analyzed *via* a fracture mechanics approach to predict adhesive failure in known geometries [9]. Unfortunately, such tests in which adhesive failure initiates at an air–polymer–substrate

"corner" are ill-suited for determining the critical values of the normal and tangential surface traction in encapsulated components because of very nonuniform stresses at the initiation site (imparting unnecessary sensitivity to the constitutive equation and meshing) and uncertainty in the local geometry (radius of curvature at the substrate corner, meniscus of the adhesive, etc.)

A few tests do avoid initiation at a sharp "corner" and generate relatively smooth stress distributions. The shear napkin-ring test [10] is one such example. For a test geometry with an outer radius of 9.25 mm and an inner radius of 8.25 mm, the shear stresses vary by only 2% within the sample), and the local surface traction is approximated well by the macroscopic torque divided by the mean radius and sample area. The cruciform tensile test [11] is another sample geometry that attempts to avoid stress concentrations. Here, the tensile stress on the embedded cylindrical substrate is somewhat uniform in the center of the sample. However, a common deficiency of both tests is the inability to accommodate mixed modes of loading. For example, a tensile stress applied to the napkin-ring test now generates a singularity at the air–polymer–substrate corner that is similar to that seen in the butt tensile test.

3.2. A New Test

We desire a new test that incorporates four key features: (1) adhesive failure initiates away from an air interface, (2) the stress distribution near the initiation site is slowly varying (*i.e.*, not highly concentrated as in a butt tensile test), (3) the thermal residual stresses are not dominant, and (4) mixed mode testing is enabled. Figures 2 and 3 show a test geometry that fulfills all four requirements. Each specific feature of this unusual shape is crucial to ensuring uniform stress distributions. For example, the material interface is a smoothly varying surface that is flat on the bottom near the axis of symmetry and curved along the outer radial dimensions. The curved edges and the "overhanging" polymer are needed to prevent a high stress gradient at an otherwise sharp corner. Under tension, the maximum interfacial traction is located on the axis of symmetry and varies only slightly along the flat bottom. In torsion, the interfacial shear strain increases with radial distance from the axis of symmetry and is inversely proportional to the separation between substrates. Through a choice of the spacing, curvature, and size of the "overhanding" polymer, the location of the maximum shear strain can be positioned in the lower part of the curved surface away from the air interface. It is clear that rational design of this geometry requires computational modeling. Details of the finite-element analyses performed in this study are presented in

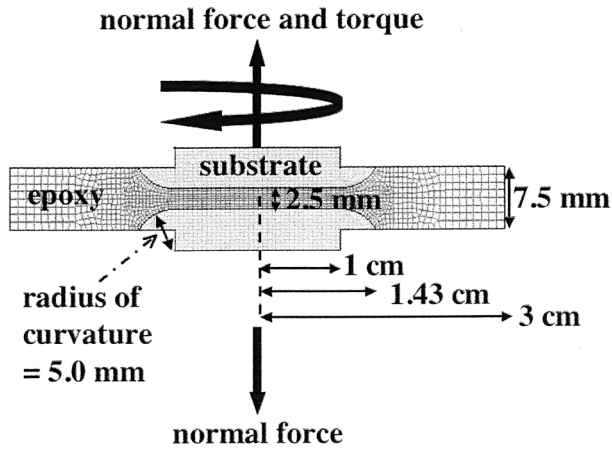

FIGURE 2 Cross section of the new test geometry.

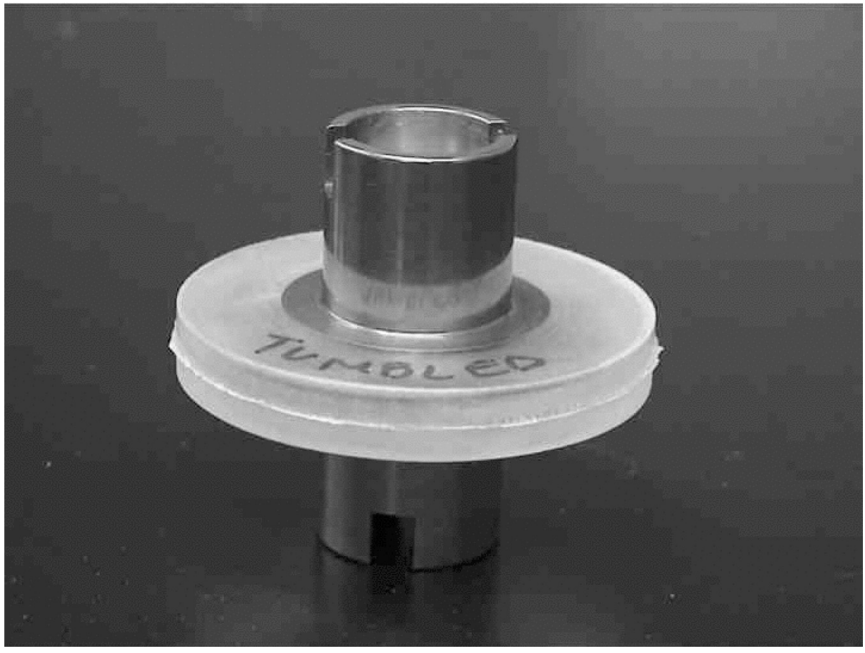

FIGURE 3 Photograph of an actual test specimen with the new geometry.

TABLE 1 Elastic Constants Used in the Computational Design of the New Test Geometry

Property	Substrate	Epoxy
Young's modulus (GPa)	195	2.14
Poisson's ratio	0.272	0.427
Linear coefficient of thermal expansion (ppm/C)	17.2	64

Appendix A. A simple elastic model for the epoxy is sufficient to locate the position of the maximum tractions and determine sensitivities of the test results to geometrical variations. Table 1 lists the elastic constants used for the epoxy and substrate for these sensitivity studies.

A cross section of a typical finite-element mesh used to design the test geometry is shown in Figure 2. Four types of analyses were performed: tension, torsion, thermal cooldown, and mixed mode. These were chosen to identify the location of the maximum interfacial traction and to assess the importance and contribution of the thermal residual stresses for a given geometry. The thermal residual stresses were based on cooling 50°C from a stress-free state. Figures 4 and 5 contain plots of

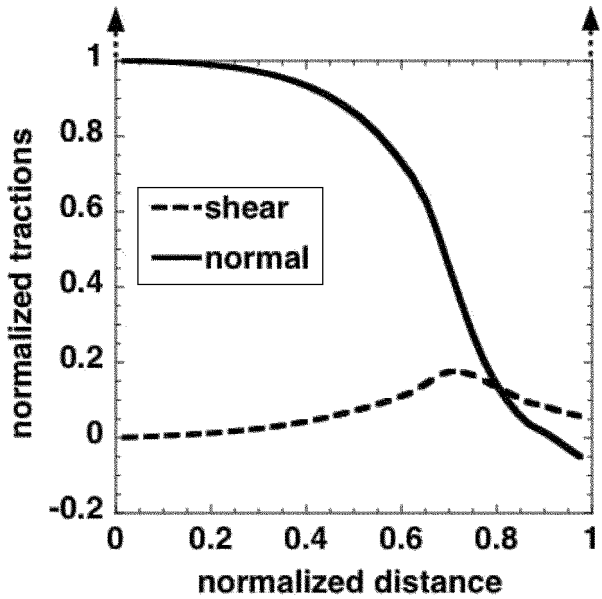

FIGURE 4 Normalized shear and normal tractions in the new test geometry across the face of the substrate during a tensile test.

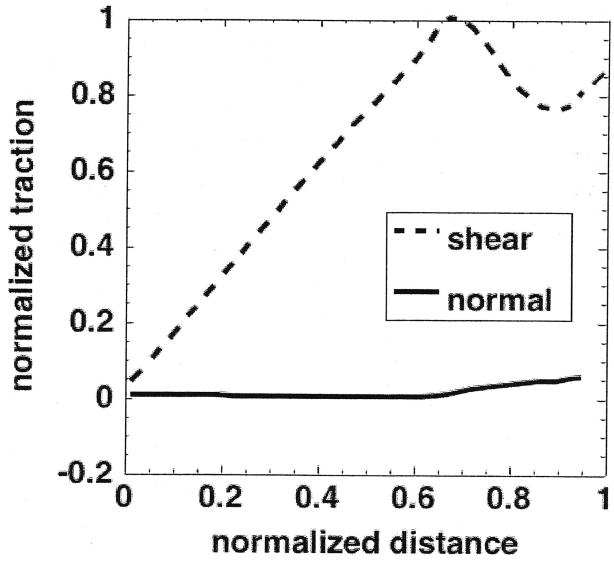

FIGURE 5 Normalized shear and normal tractions in the new test geometry across the face of the substrate during a torsion test.

the interfacial tractions obtained from isothermal elastic tension and torsion tests, respectively, for the optimal geometry. The shear and normal tractions at the substrate polymer interface are plotted as a function of the distance along the substrate measured from the axis of symmetry. To pinpoint the location of the maximum traction, all values were normalized by the magnitude of the largest component of the traction in the problem. As desired, the maximum tractions are located at some distance away from the air interface. To investigate the effects of thermal residual stresses, the tension test was analyzed after a thermal cooldown. Figure 6 contains the results from the temperature change only, and Figure 7 shows the values obtained by combining thermal and tension loading. Tractions in both figures were normalized using the magnitude of the maximum traction from the combined thermal and tension loading. The contribution from thermal stresses is quite small; for example, thermal stresses in a tensile test add roughly 0.1% to the normal traction for every degree Centigrade. The tractions from a coupled tension/torsion test (0.6% tensile strain and 1% shear strain) are shown in Figure 8. The shape of the normal and shear tractions are very similar to the uncoupled results shown in Figures 4 and 5.

Although the preceding analyses could employ elastic material models to assess geometrical sensitivities, analyses of the actual adhesion

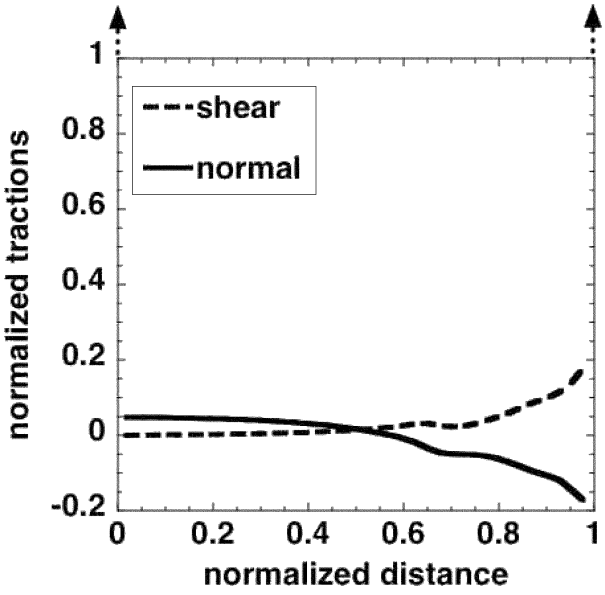

FIGURE 6 Normalized shear and normal tractions in the new test geometry across the face of the substrate after cooling 50°C from a stress-free state.

tests require higher fidelity models models to be quantitative. As is discussed later, mechanical yield (*i.e.*, a maximum in the stress during a constant strain rate ramp) can occur in the polymer during the tests. Because this yield in polymers is quite dependent upon the temperature, rate, and mode of deformation, it is imperative to employ a material model capable of accurately reproducing this response. We recently developed a nonlinear viscoelastic model that has been validated on several polymer systems. Behavior ranging from physical aging to enthalpy relaxation to mechanical yield was predicted accurately with one consistent parameter set for each material. Moreover, each parameter set is physically based and deduced from simple and standard linear viscoelastic tests. A brief discussion of this approach is given in Appendix B, but the interested reader should refer to the original articles [1, 2] for much greater detail.

4. DATA

4.1. Experimental System

The epoxy adhesive used in this study consists of the diglycidyl ether of bisphenol A (DGEBA, Epon® 828 from Resolution Products, Houston,

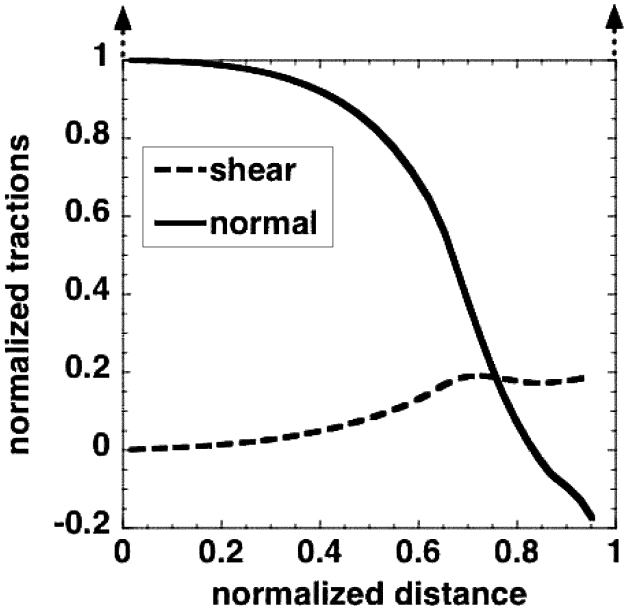

FIGURE 7 Normalized shear and normal tractions in the new test geometry across the face of the substrate during a tensile test after cooling 50°C from a stress-free state.

TX, USA) cured with diethanolamine (DEA, Fisher Scientific, Hampton, NH, USA) at a ratio of 100 to 12 parts by weight (pbw). Samples were mixed, degassed, and cured at 90°C for 48 h, resulting in a relatively low glass transition temperature of 65°C. The cure mechanism of this system is quite complex and slow. At 90°C, the secondary amine of DEA completely reacts in 5 min to endcap roughly half of the DGEBA. Because the gel time occurs in about 3 h, it is clear that the cross-linking mechanism involves species other than the secondary amines. At temperatures less than 70°C, this cross-linking mechanism occurs primarily by the tertiary amine-catalyzed condensation of the epoxy with primary or secondary alcohols, whereas at temperatures greater than 110°C, the tertiary amine-catalyzed epoxy homopolymerization becomes increasingly important. At intermediate temperatures, both reactions occur. Nevertheless, the change in all thermophysical properties with cure can be reasonably correlated with the empirical extent of reaction, defined as the fraction of epoxies reacted.

The substrate plugs were machined from 304 stainless steel. Processing lore suggests it is more difficult to ensure proper bonding to

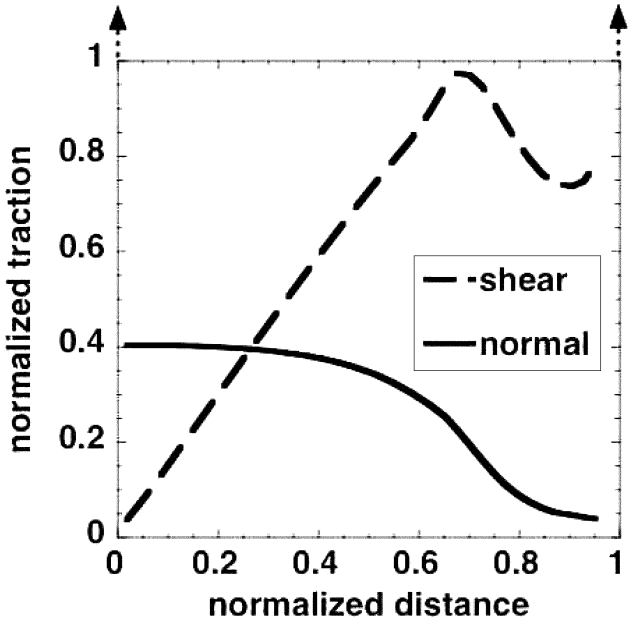

FIGURE 8 Normalized shear and normal tractions in the new test geometry across the face of the substrate during a coupled tension/torsion test.

stainless steel than such substrates as aluminum and unhardened steel. The plug surfaces were either tumble-polished or sand-blasted followed by an alcohol rinse in the studies described here. Preparing samples of the required shape (Figures 2 and 3) was not as difficult as might be anticipated. Two Teflon® half-molds were fabricated such that the plug of the metal substrate protruded out of each half (Figures 9 and 10). Fill holes were drilled into the mold halves, and the epoxy was thoroughly degassed after both reactant mixing and mold filling. The epoxy was cured at 70°C for 16 h. Ramped tensile tests were conducted on an Instron 1125 (Instron, Norwood, MA, USA) axial load frame at a rate of roughtly 20×10^{-6} m/s (0.05 in./min). Ramped torsional tests were conducted on an axial/rotational Instron load frame at a rate of 5 deg/min.

The complex response of this glassy polymer was modeled with the previously mentioned nonlinear viscoelastic constitutive equation [1]. The material characterization process for the epoxy is thoroughly detailed in Ref. 2, and the model parameters for the 828/DEA epoxy are listed in Table 6 of that article. A brief description is presented in Appendix B.

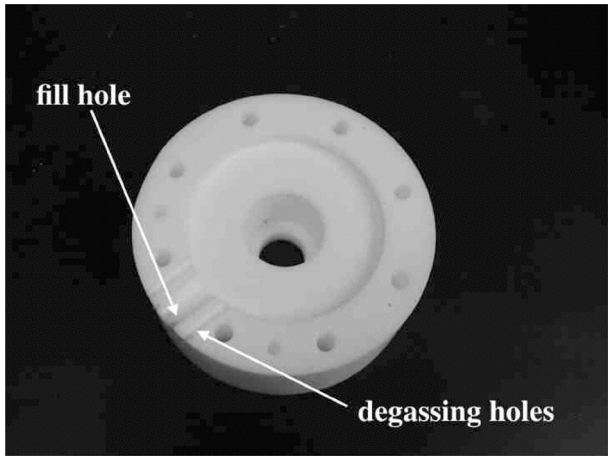

FIGURE 9 Photograph of a mold half used for preparing the new test specimens.

A few tests were conducted using the historical napkin-ring geometry for comparison with the new test geometry in shear only. The lower face of our napkin-ring tests was simply a flat, stainless steel plug 2.54 cm (1 in.) in diameter. The upper face had a 1.65 cm (0.65 in.) I.D./1.9 cm (0.75 in.) O.D. ring machined onto the flat,

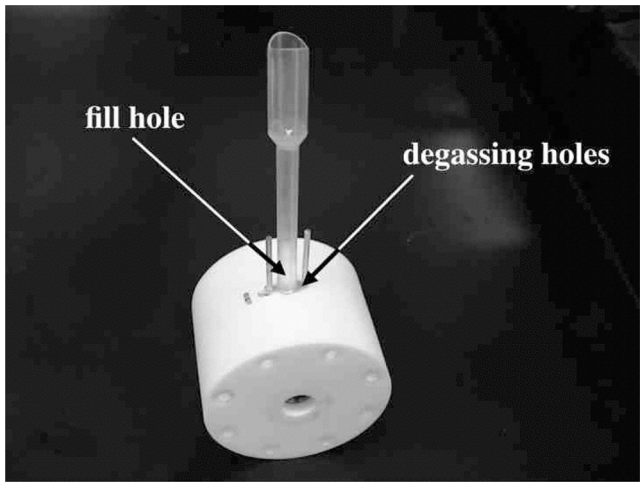

FIGURE 10 Photograph of an assembled mold used for preparing the new test specimens.

stainless steel plug. Again, both faces were alcohol rinsed prior to curing the epoxy at 70°C for 16 h. The gap was kept constant during cure at 0.025 cm (0.01 in.) by a spacer that was removed after cure. Ramped torsional tests were run on an Instron axial/torsional load frame at a rate of 5 deg/min.

4.2. Adhesive Test Results

The initiation of failure in tensile or torsional tests was catastrophic. In fact, the samples stored so much energy that failure was an unmistakable event in the laboratory. It would have been advantageous to have measured and recorded accurate load-displacement traces for each test. Unfortunately, although the loads were easily resolved, the displacements were almost imperceptible. For example, a tensile strain of 5% over a gap of 1 mm results in a displacement of only 50 microns. Even in the historical napkin-ring test used in these some of these studies, a shear strain of 5% occurs at an angular displacement of less than 0.1 deg. Therefore, we are only able to report loads at failure reliably.

Test results for pure tensile ramps on polished surfaces at temperatures of −40, −10, 23, 38, and 50°C, which range from 20°C to over 100°C below the glass transition (roughly 70°C), are shown in Figure 11. Both the measured load at failure and computed critical normal traction are plotted. The critical normal traction was identified from the finite-element analyses at the measured load at failure. The difference between the temperature dependencies of the two values lies in the slight effect from thermal cooldown stresses. For clarity, all load-at-failure data are presented but only average values of the critical traction are shown with error bars representing the range of values extracted from the data. The critical traction appears sensitive to temperature only near the glass transition. Representative failure surfaces are shown in Figures 12 and 13. The surfaces of samples tested at 50°C (Fig. 12) appear totally free of polymer as would typically be associated with "adhesive" failure. The surfaces of samples tested at lower temperature (*e.g.*, −10°C in Fig. 13) clearly initiate failure at the surface near the center of the disk as predicted, yet much polymer still clings to the surfaces. A closer view of the initiation site is shown in Figure 14 and is free of polymer.

The results for torsional ramps on polished surfaces as a function of test temperature (0, 23, and 36°C) are shown in Figure 15. Also shown in Figure 15 are comparable results using the historical napkin-ring test described previously. The size of the symbols now represents the scatter in the range of values obtained at each

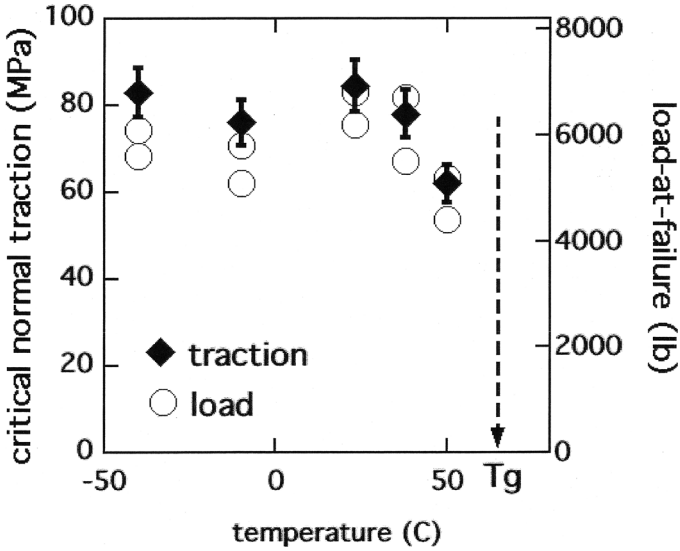

FIGURE 11 Computed critical normal tractions and experimental loads at failure in the new test geometry for tension ramps at different temperatures.

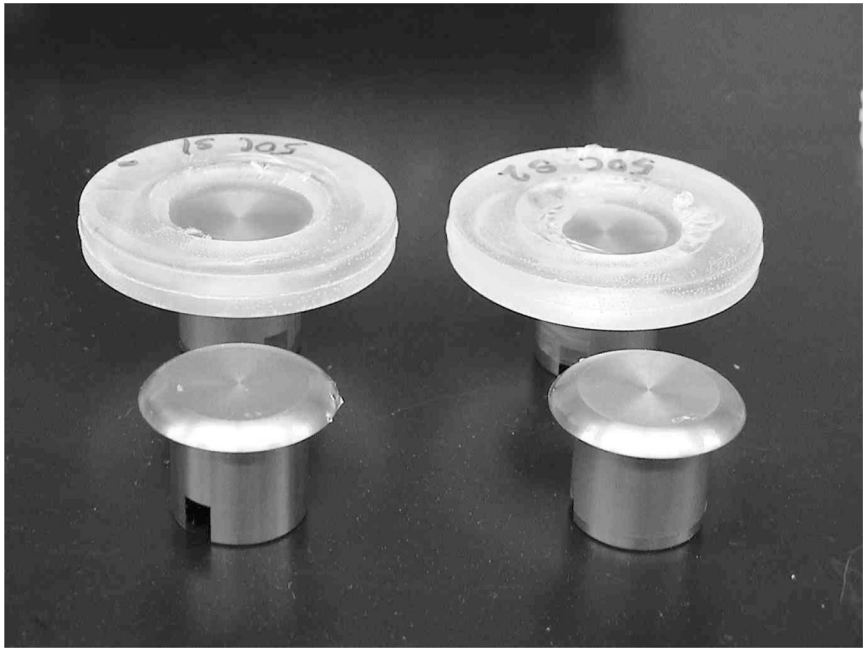

FIGURE 12 Photo of failure surfaces in tensile ramp tests at 50°C.

FIGURE 13 Photo of a failure surface in a tensile ramp tests at –10°C.

temperature, and the two tests yield similar results. Failure surfaces for these shear tests are shown in Figure 16, and in this case, the surfaces are clean.

Included in Figures 17 and 18 are the results for tensile and torsional (in both new and napkin-ring geometries) deformations respectively on sand-blasted surfaces. There seems to be no significant effect of surface roughening on the initiation of adhesive failure for this epoxy–substrate pair. We return to discuss this observation in the next section.

Finally, the results of a mixed-mode test are compared with those from torsion-only loading in Figure 19. Here, a compressive load of 909 kg (2000 lbs) (roughly one third of the critical tensile load for failure) was applied to the new test sample with roughened surfaces followed by a torsional ramp of 5 deg/min. One might think that a rather large normal load might lead to an increase in the critical tangential traction, especially for roughened surfaces. However, the results of Figure 19 show little effect. If anything may be inferred, it appears that the normal load actually decreases the critical tangential traction.

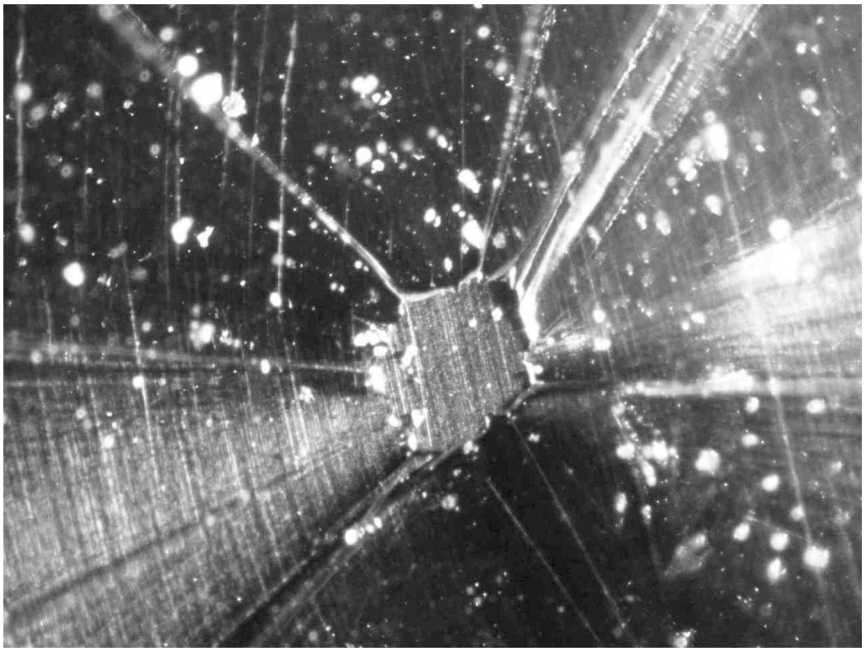

FIGURE 14 Close-up of the initiation site in Figure 12.

5. DISCUSSION

5.1. Different Temperature Dependencies of the Normal and Tangential Critical Tractions

From Figures 11 and 15, the normal critical traction has no significant temperature dependence whereas the tangential critical traction appears to increase as temperature decreases. To understand this difference, stresses in the actual test geometry were computed using the nonlinear viscoelastic constitutive equation described previously [1, 2] and summarized in Appendix B. Figure 20 plots the maximum principal stress in the entire geometry during a tensile ramp as a function of the applied load after cooldown from the glass transition temperature to the test temperature. Mechanical yield is apparent (the deviations from linearity), and the yield stress increases as temperature decreases. It is important to realize that the magnitude of the yield stress in these tests is much larger than the calculated or measured yield stresses in simple "dogbone" tensile tests, because the lateral confinement in the two tests is quite different. Similar calculations

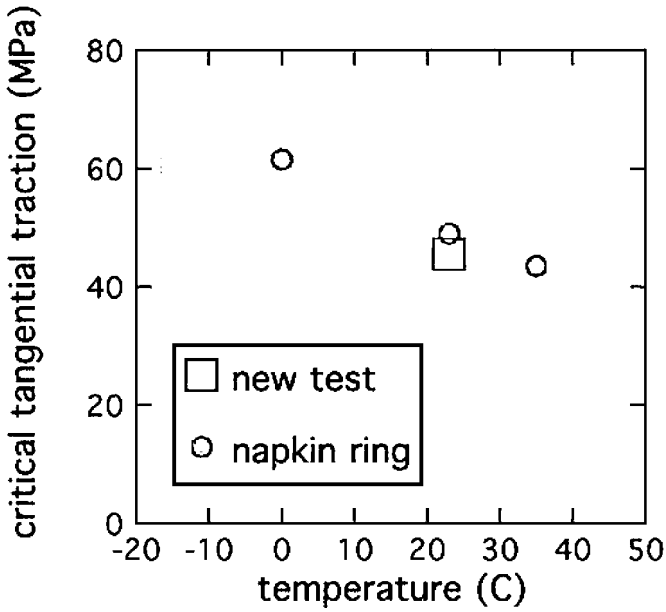

FIGURE 15 Critical tangential tractions in the new test geometry and in the napkin-ring geometry for torsion ramps at different temperatures.

FIGURE 16 Photo of a failure surface in a torsional ramp test.

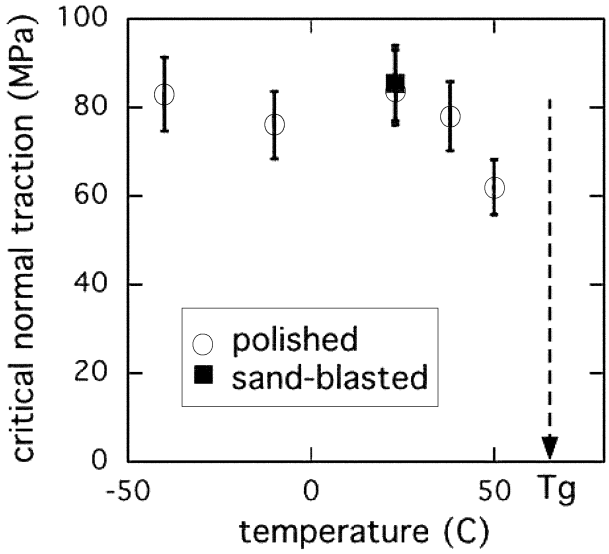

FIGURE 17 Critical normal tractions in the new test geometry with polished or sand-blasted surface finishes for tension ramps at different temperatures.

of the yield stress were performed for the torsional ramps in both the new and napkin-ring geometries.

The yield stress in the epoxy at the point of maximum principal stress is plotted in Figure 21 as a function of temperature along with the critical tractions for both tensile and torsional tests. Two points need to be highlighted. First, the critical normal traction is much less than the computed yield stress in the epoxy during tensile tests. Therefore, failure occurs prior to yield in the tensile tests. Second, the critical shear traction by contrast coincides with shear yield in the epoxy in torsional tests, so failure in shear occurs at yield in these ramp-to-fail tests. It is not surprising, then, that the tension and shear critical tractions have different temperature dependencies.

5.2. The Critical Traction for Rough Surfaces is not Greater than for Smooth Surfaces

It was surprising to us that sand-blasting had little effect on the critical tractions for the initiation of adhesive failure. Common practice suggests that surface roughening will improve adhesion. Several points must be made here. First, it is important to distinguish true

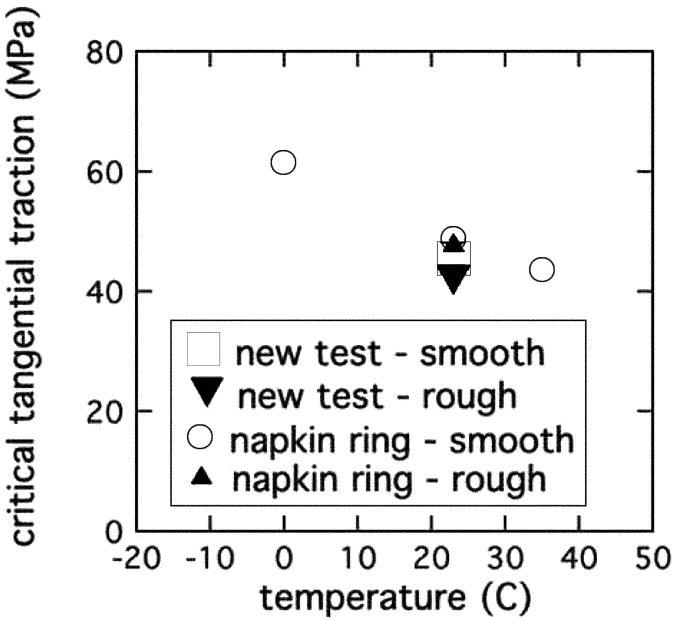

FIGURE 18 Critical tangential tractions in the new test geometry and napkin-ring geometry with polished or sand-blasted surface finishes for torsion ramps at different temperatures.

surface roughening that accompanies sand-blasting *versus* improved surface cleaning that can accompany sand-blasting. Second, roughening of any kind may actually change the surface chemistry and, therefore, affect adhesion. However, substrates such as aluminum or steel reform their oxide coatings so quickly that sand-blasting should have little chemical effect. Third, although sand-blasting does not seem to affect the initiation of adhesive failure, it may indeed affect the propagation of an existing surface crack. Fourth, most systematic studies of the effect of surface roughening employ butt tensile or lap shear test geometries [12], where adhesive failure initiates at the substrate corner and the magnitude of the load at failure is very sensitive to the radius of curvature at the corner [9]. Sand-blasting may smooth sharp corners, thus increasing the radius of curvature and measured load at failure. Finally, it is unclear upon further reflection that sand-blasting should postpone the initiation of adhesive failure. Examine the stresses in an epoxy adjacent to a smooth surface and a rough surface. Unarguably, the stresses at

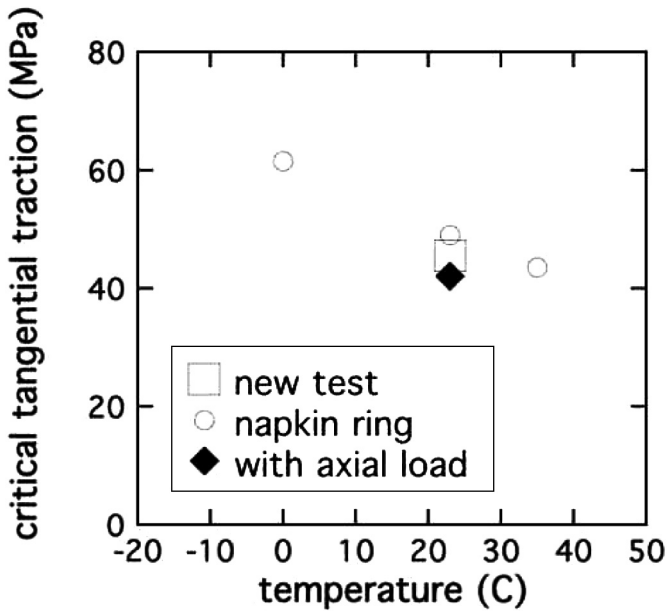

FIGURE 19 Comparison of the critical tangential traction for pure torsion ramps and mixed mode loading (torsion ramp under a compressive load) in the new test geometry.

the roughened surface will be greater for a given applied load because the jagged features act as stress concentrators. Therefore, if one postulates a local stress-based metric for the initiation of adhesive failure that then propagates catastrophically, sand-blasting should actually degrade adhesion.

So why do the data show almost no effect from sand-blasting? To begin addressing this question, simple calculations of idealized, roughened surfaces were performed where the roughness was modeled as shown in Figure 22. Each peak "tip" was given a radius of curvature, and the ratio of peak height, H, to peak-to-peak length, L, was specified. Several model parameter sets were investigated (Fig. 23). The epoxy and substrate were modeled elastically with the parameters in Table 1 with symmetrical side boundary conditions. For tensile tests, failure was identified as the point at which the traction somewhere on the surface equaled a critical normal traction. For a perfectly smooth surface, $H/L = 0$, the macroscopic stress at failure would equal the assumed magnitude of the critical normal traction. For rough surfaces, however, the macroscopic stress at failure would decrease because

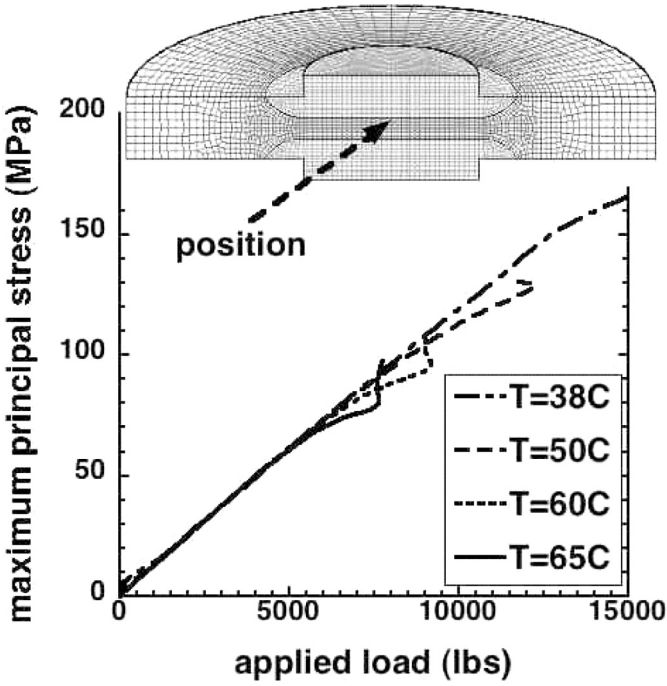

FIGURE 20 Maximum principal stress in the new test geometry during tension ramps at different temperatures. The polymer clearly yields.

the peaks act as stress concentrators. This trend is presented in Figure 24. It is somewhat surprising that surface roughness does not profoundly affect the failure stress. A surface for which $H/L = 1$ is quite rough indeed; yet, the failure stress decreases only by 40%. Because our polished surfaces are not optically smooth, perhaps the "smooth" surface experimental results actually correspond to those calculated for a slightly roughened surface. The decrease in failure stress due to the additional roughness from sand-blasting may lie within the experimental scatter.

6. CONCLUSIONS

Predicting the initiation of adhesive failure at embedded interfaces directly from finite-element analyses requires accurate geometrical meshing, high-fidelity constitutive equations, and metrics for determining the critical stress levels at which delamination occurs. The test requirements to determine these initiation metrics are much different

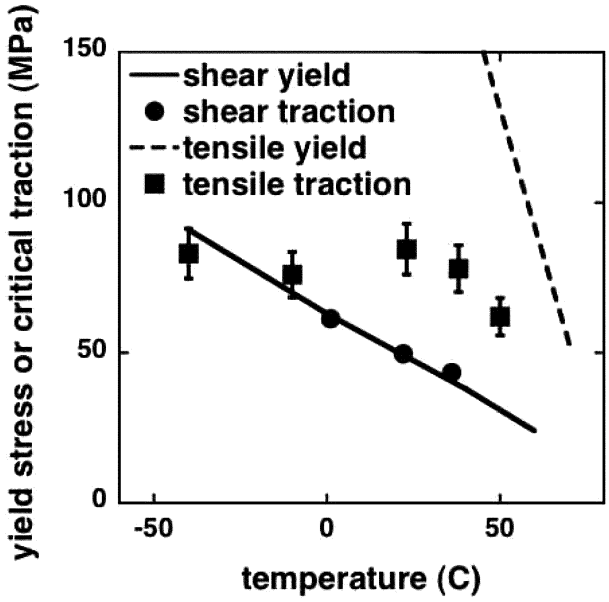

FIGURE 21 Computed tensile and shear yield stresses as a function of temperature are compared with the experimental normal and tangential critical tractions from tension and torsion ramps.

from those for measuring the propagation of an existing surface crack. Few existing test geometries are suitable for such investigations, so we designed a new test that avoids initiation near an air interface,

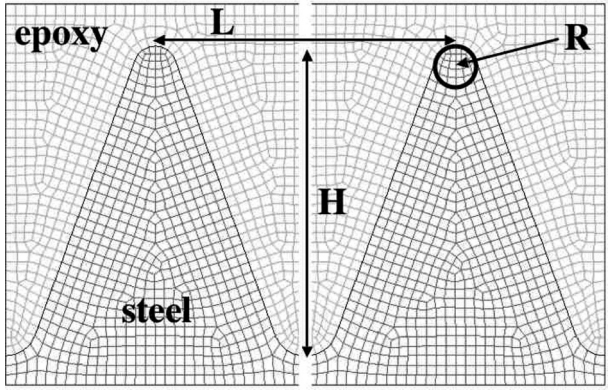

FIGURE 22 Idealization of surface roughness for finite-element calculations.

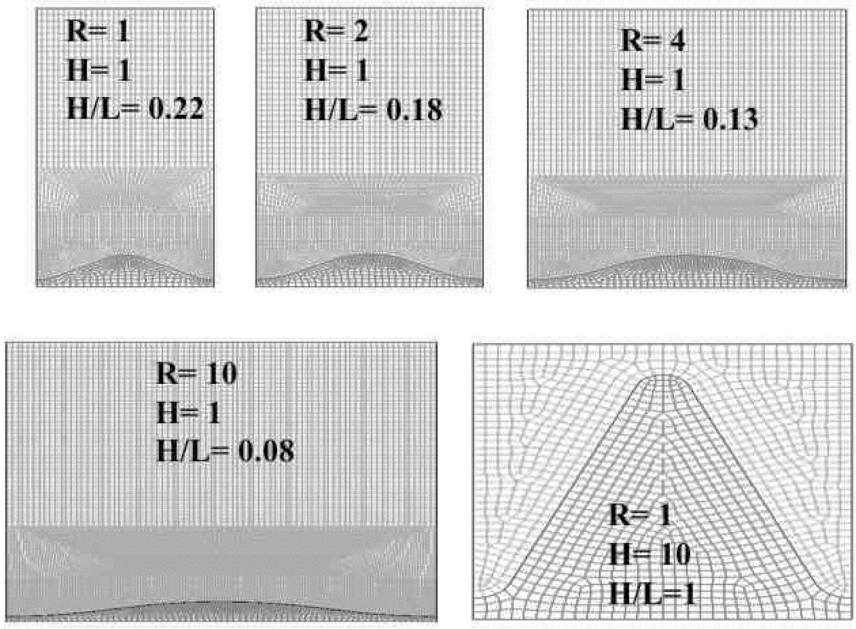

FIGURE 23 Various types of model surface roughness were investigated with finite-element analysis.

singular stresses at the initiation site, and excessive residual thermal stresses. In addition, mixed-mode testing is enabled. Although sample preparation is not as trivial as for standard butt tensile or lap shear, it is not too demanding, and a simple mold design was presented. The design details as well as the calculation of the surface tractions in each test were defined using finite-element analysis. Such modeling is not only key to revealing optimal test geometries but is necessary to analyze test results. The willingness to solve a boundary value problem as part of the experimental process allows one to use a more complicated specimen geometry to avoid more complicated (*i.e.*, singular) stress distributions. In today's computational environment, it will and should be more commonplace for numerical calculations to be an integral part of material characterization tests.

Results using the new test geometry were at times surprising. For an epoxy adhered to stainless steel, where adhesion is supposedly somewhat difficult, initiation of adhesive failure in shear was linked to yield in the bulk epoxy. Even more unexpectedly, sand-blasted surfaces appear to fail at approximately the same applied load as polished surfaces.

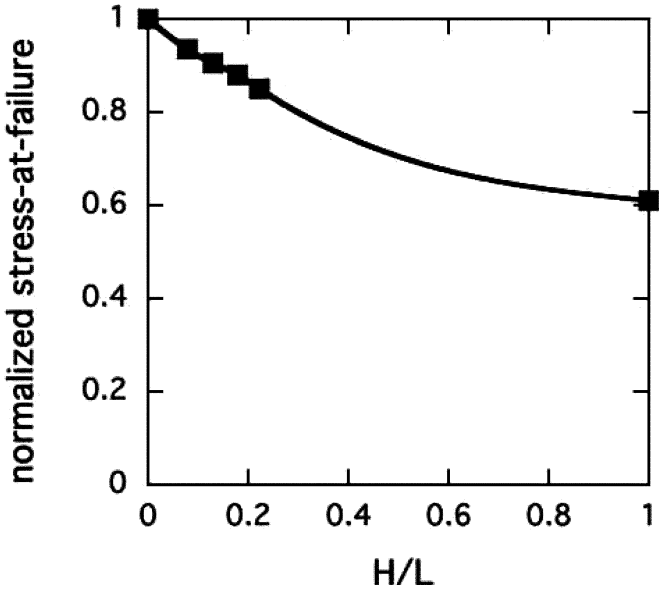

FIGURE 24 The macroscopic stress at failure is predicted to decrease as surface roughness increases.

APPENDIX A: FINITE ELEMENT ANALYSES

All the stress analyses were performed using the ADAGIO finite-element code (in-house software developed at Sandia National Laboratories, NM). ADAGIO is a three-dimensional implicit quasi-statics and dynamics code with a versatile element library, nonlinear material models, large deformation capabilities, and contact. It is built on the SIERRA framework, providing a data management framework for parallel computing. The finite-element meshes were generated using eight-node uniform strain elements with single-point integration and hourglass controls. To analyze the loadings on the test specimen with optimal efficiencies, two meshes were created. A view of the typical finite-element cross section is provided in Figure 2. The first mesh employed three symmetry planes (1/8 of total model) corresponding to each of the three global coordinate planes, one through the center of the epoxy thickness perpendicular to the longitudinal axis of symmetry, and two others cutting out one quarter of the cylindrical section in a 90-deg wedge. This model was suitable for tension and compression loadings. It consisted of 14031 nodes and 11840 elements with four elements through the epoxy half-thickness (from metal to

symmetry plane). The second mesh was based on a comparable spatial discretization but encompassed the entire geometry including the entire top and bottom metallic saucers as well as the entire epoxy disk. This model was substantially larger, having 97917 nodes and 92800 elements. It was used for the torsional and combined axial load cases. Sixteen elements were employed in the definition of the curved boundary defining the outer surface of the metallic saucer. This degree of mesh refinement was chosen to capture the geometric shape after performing successive analyses doubling the number of elements in the model to assess the impact on numerical predictions. The more refined mesh was chosen after determining that potential spatial discretization errors fell well within the scatter of the experimental results. The ADAGIO solutions were obtained through a conjugate gradient algorithm that enforces the momentum balance by minimizing the force residuals. Convergence was defined by requiring the relative residual tolerance to be less than or equal to $1.0E^{-4}$ (based on the ratio of the net residual to the L2 norm of the total reactive force).

Because epoxies are viscoelastic materials with fading memory, it is important to capture their evolving history. All analyses were initiated at the annealing temperature of 75°C (about 10° above the glass transition temperature). Samples then were cooled to the test temperature at 0.5°C/min, and the thermal residual stresses and strains were computed as the starting state for the imposed mechanical loading. Aside from the normal displacement boundary conditions imposed on symmetry planes, rigid body constraints and loadings were applied to the axial ends of the metallic saucers through imposed displacements. In tension, axial motion of 1.27 cm/min (0.05 in./min) was prescribed and in torsion a cylindrical rotation (5 deg/min) about the longitudinal axis was enforced. During cooling, 0.25°C temperature steps were taken through the glass transition followed by 0.5°C steps to the test temperature. The time discretization through loading (0.125 s/step axial and 0.5 s/step torsion) was designed to produce a comparable change (0.13%) in the infinitesimal strains at the point of expected failure. This was chosen to be conservative based on prior experience in analyzing complex deformations through yielding.

APPENDIX B: POLYMER CONSTITUTIVE EQUATION

Although the new test geometry presented in this article allows extraction of the critical normal and tangential tractions defining the initiation of adhesive failure, the process requires finite-element analysis of the test and an accurate constitutive equation for the polymer. Critical tractions at different temperatures in different (even mixed)

modes of deformation must be evaluated, so the constitutive equation must be valid over this broad range of test conditions. In previous articles [1, 2], we developed and validated the only current polymeric constitutive equation that is capable of such broad quantitative predictions. A brief description of the equation is presented in this appendix. Much more detail concerning the foundation of the approach, the characterization tests, the process for parameter population, and the experimental validation tests are given in the original articles.

The approach accepts the viscoelastic nature of polymers and understands the need for thermodynamic consistency. Therefore, following the rational mechanics framework [13], the Helmholtz free energy is assumed to depend on the strain and temperature histories and is expanded in a Frechet series (a functional Taylor series) in these histories. Nonlinear phenomena such as mechanical yield arise from the dependence of the "material clock" on the potential energy of the system. That is, polymer relaxation rates are accelerated by an increase in the system's free energy. Because the potential energy increases as the temperature increases above the glass transition temperature (T_g), the potential energy clock can reproduce the well-known "WLF" temperature dependence of the viscoelastic shift factor. In the glassy polymer, the potential energy increases during a strain ramp, and relaxation rates will continually accelerate until yield occurs.

The simplest form of the constitutive equation appears very similar to standard linear viscoelastic equations:

$$\begin{aligned}\underline{\mathrm{S}}_{\mathrm{H}} = &\left[(K_{\mathrm{g}} - K_{\mathrm{r}}) \int_0^{\mathrm{t}} \mathrm{d}s f_{\mathrm{K}}(\mathrm{t}^* - \mathrm{s}^*) \frac{\mathrm{d}I_{\mathrm{H}}}{\mathrm{d}s} \right.\\ &\left. -(K_{\mathrm{g}}\alpha_{\mathrm{g}} - K_{\mathrm{r}}\alpha_{\mathrm{r}}) \int_0^{\mathrm{t}} \mathrm{d}s f_{\alpha}(\mathrm{t}^* - \mathrm{s}^*) \frac{\mathrm{d}T}{\mathrm{d}s}(\mathrm{s})\right] \underline{\mathrm{I}}\\ &+ 2(G_{\mathrm{g}} - G_{\mathrm{r}}) \int_0^{\mathrm{t}} \mathrm{d}s f_{\mathrm{G}}(\mathrm{t}^* - \mathrm{s}^*) \frac{\mathrm{d}\left(\underline{\mathrm{H}} - \frac{1}{3} I_{\mathrm{H}} \underline{\mathrm{I}}\right)}{\mathrm{d}s}\\ &+ [K_{\mathrm{r}} I_{\mathrm{H}} - K_{\mathrm{r}}\alpha_{\mathrm{r}}(T - T_{\mathrm{ref}})]\underline{\mathrm{I}} + 2G_{\mathrm{r}}\left(\underline{\mathrm{H}} - \frac{1}{3} I_{\mathrm{H}} \underline{\mathrm{I}}\right) \end{aligned} \tag{A1}$$

K_{g}, G_{g}, and α_{g} are the glassy (below T_{g}) bulk modulus, shear modulus, and coefficient of thermal expansion (CTE), and K_{r}, G_{r}, and α_{r} are the corresponding rubbery (above T_{g}) properties. There are three independent relaxation functions, f_i, that depend on the reduced time interval,

$$t^* - s^* = \int_{\mathrm{s}}^{\mathrm{t}} \frac{\mathrm{d}u}{a(E_{\mathrm{pot}}(u))}, \tag{A2}$$

where the viscoelastic shift factor, a, depends on the system potential energy as stated above. Because the constitutive equation uses the logarithmic Hencky strain measure, $\underline{H}$ (I_H is its trace and is a function of the volumetric strain), the stress defined in Equation (A1) is conjugate to $\underline{H}$. Therefore, the Cauchy stress required for the momentum balance is found by

$$\underline{\sigma} = \frac{\rho}{\rho_{\text{ref}}} \underline{F} \cdot \left[\underline{S}_H : \frac{d\underline{H}}{d\underline{E}} \right] \cdot \underline{F}^T \tag{A3}$$

where $\underline{F}$ is the deformation tensor, ρ is the density, and $\underline{E} = (\underline{F}^T \underline{F} - \underline{I})/2$ is the Green–Lagrange strain measure. Equation (A1) becomes more complicated if the moduli and CTE depend on temperature and/or volume. Note that the model parameters of Equation (A1) are familiar quantities (moduli and CTE) that can be easily defined by standard lab tests.

In Ref. 2, we demonstrated that the predictions of this model for a variety of tests ranging from enthalpy relaxation to temperature-dependent yield to physical aging were quantitative. Note that competing models have fundamental flaws in the ability to predict a broad range of phenomena accurately using one consistent set of input parameters. For example, free volume and configurational entropy theories can predict enthalpy relaxation but cannot predict any yield in compression. Plasticity theories can predict yield by construction but cannot predict any enthalpy relaxation or physical aging. Stress and strain clocks have similar limitations. In addition, such models require model parameters that are not tied to linear phenomea (*e.g.*, the "strength" of the strain clock), whereas the model parameters of Eq. (A1) are constrained by linear viscoelastic tests.

REFERENCES

[1] Caruthers, J. M., Adolf, D. B. Chambers, R. S., and Shirkande, P., *Polymer* **45**, 4577–4597 (2004).
[2] Adolf, D. B., Chambers, R. S., and Caruthers, J. M., *Polymer* **45**, 4599–4621 (2004).
[3] Knott, J. F., *Fundamentals of Fracture Mechanics* (Butterworths, London, 1973), Chap. 6, pp. 150–175.
[4] Needleman, A., *J. Appl. Mech*. **54**, 525–531 (1987).
[5] Wei, Y. and Hutchinson, J. W., *Int. J. Fracture* **93**, 315–333 (1998).
[6] Yang, Q. D., Thouless, M. D., and Ward, S. M., *J. Mech. & Phys. Solids* **47**, 1337–1353 (1999).
[7] Mohammed, I. and Lechti, K. M., *J. Mech. & Phys. Solids* **48**, 735–764 (2000).
[8] Reedy, E. D., Mello, F. J., and Guess, T. R., Sandia National Laboratories Reports, SAND95-3070J (Albuquerque, NM, 1995).
[9] Reedy, E. D. and Guess, T. R., *J. Adhes. Sci. & Tech*. **9**, 237–251 (1995).

[10] Bossler, F. C., Franzblau, M. C., and Rutherford, J. L., *J. Physics E* **1**, 829–833 (1968).
[11] Tandon, G. P., Kim, R. Y., Warrier, S. G., and Majumdar, B. S., *Composites: Part B* **30**, 115–134 (1999).
[12] Jennings, C. W., *J. Adhes*. **4**, 25–37 (1972).
[13] Coleman, B. D., *Arch. Rat. Mech.* **1**, 17 (1964).